

# A Crystallographic Basis for Critically Evaluating the Mechanisms for Secondary Grain Formation During Directional Solidification



N. D'SOUZA, I.M. EDMONDS, M. PERRY, and D.M. COLLINS

A crystallography-based method is presented for the critical appraisal of possible mechanisms that trigger the formation of secondary grains during directional solidification. The method permits an analysis of a large population of defects, while avoiding the pitfalls of the metallographic sectioning approach that is affected by dendrite stereology. Here, the nickel-base superalloy CMSX-4, an alloy commonly used for single crystal turbine blade applications, is studied. All secondary grains originate exclusively at the external surface and when the off-axial primary  $\langle 001 \rangle$  crystal orientations are measured, are evident at both the converging and diverging dispositions of the single crystal primary dendrites without a noticeable bias. Almost all of the secondary grains have low misorientations, with an average misorientation between 5 to 15 deg. No systematic deviation between the individual  $\langle 001 \rangle$  orientations of the secondary grain and the single crystal is observed. A significant twist contribution about an axis within  $\sim 30$  deg from one of the secondary arms occurs when primary arms converge on the external surface, but both twist and tilt prevail for the diverging case. Both nucleation and buoyancy driven thermo-solutal convection can be eliminated as potential mechanisms. Thermo-mechanical deformation is deduced to be the most likely mechanism; deformation must originate in the vicinity of the primary dendrite tips. It is proposed that dendrite deflection arises primarily from the resistance encountered by the primary tips with the external surface during axial contraction in the presence of a dominant vertical thermal gradient.

<https://doi.org/10.1007/s11661-023-07194-7>

© The Author(s) 2023

## I. INTRODUCTION

SINGLE crystal (SX) turbine blades are routinely manufactured using the state-of-the-art investment casting method, where a directional thermal gradient is maintained perpendicular to the solid/liquid interface.<sup>[1]</sup> For the manufacture of nickel-base superalloy turbine blades, a spiral grain selector is used to grow a single grain, from amongst the many, with an axial orientation close to  $\langle 001 \rangle$ .<sup>[2]</sup> The formation of secondary grains during casting constitutes one of the principal foundry defects; this is nonconformity and significantly impacts the process economics. These defects can be broadly classified based on the mechanism for their formation:

- (a) Low angle boundaries (sub-grains) typically less than  $\sim 3$  deg and are referred to as mosaicity within the dendritic structure. This has been attributed to lateral macro-segregation that alters the local dendrite tip kinetics<sup>[3,4]</sup> or stress from lattice misfit arising during  $\gamma'$  precipitation below the  $\gamma'$  solvus temperature.<sup>[5-7]</sup> Notably, it has been shown that there is a significant segregation of Re (up to 12 at. pct) at low angle grain boundaries with dislocations within the  $\gamma$  phase.<sup>[8]</sup>
- (b) Secondary grains nucleate at discontinuities within the cross-section, such as at expanding regions in the platforms of turbine blades where there is sufficient undercooling for grain nucleation. In this case, branched dendrites of the main grain have not managed to grow into this pocket of liquid before a stray grain has nucleated.<sup>[9,10]</sup>
- (c) In the presence of buoyancy related thermo-solutal convection arising from density inversion within the mushy zone, freckles (equiaxed grains with random misorientation) can form within the mush. In extreme cases, if the advected secondary dendrite fragments are able to grow within the supercooled melt above the dendrite tips, they can settle on the advancing front and even give rise to

N. D'SOUZA, I.M. EDMONDS and M. PERRY are with the Rolls-Royce plc, PO Box 31, Derby DE24 8BJ, UK. D.M. COLLINS is with the School of Metallurgy and Materials, University of Birmingham, Birmingham B15 2TT, UK. Contact e-mail: [d.m.collins@bham.ac.uk](mailto:d.m.collins@bham.ac.uk)

Manuscript submitted June 26, 2023; accepted August 30, 2023.

a columnar-to-equiaxed transition (CET), *e.g.*, in large industrial turbine (IGT) components.<sup>[11–17]</sup>

- (d) Growth of secondary arms while growing into increasingly undercooled liquid results in a cumulative build-up of misorientation and misorientations typically  $\sim 10$  deg along the length of the branched secondary arm.<sup>[18–21]</sup> This has been argued to result from body-forces, as the secondary stems are near-orthogonal to the gravity vector.<sup>[22–25]</sup>
- (e) Secondary grains have also been observed to occur across the aerofoil or root section of the turbine blades, but interestingly their spatial occurrence from prior studies suggest it is random.<sup>[26–28]</sup> There is no unequivocal theory advocated towards their formation, although current understanding is reliant on the role of thermo-mechanical deformation. There have also been suggestions that these defects result from nucleation at heterogeneities, such as oxide bi-films or pores, however, no measurement of misorientation was provided to confirm this hypothesis.<sup>[29,30]</sup> Recent in-situ observation of Ni-base superalloys using high energy X-rays has shown time-resolved deflection of dendrite stems, providing credence to the role of thermo-mechanical deformation.<sup>[31–33]</sup>

Of these mechanisms, (e) is the most important. First, secondary grains referring to (a) through (d) can be easily suppressed by minimising curvatures of the liquidus front, control of thermal gradients and cooling rates and the use of grain continuators. Second, it is only in (e) where no general consensus of the governing mechanisms. Third, owing to the random spatial occurrence of such secondary grains, their control from a non-conformance perspective is of great significance. There is an added complexity; it is difficult to create the experimental conditions to consistently produce these secondary grains (their occurrence appears to be stochastic). To obtain a statistically reliable population of castings with secondary grains, it is necessary to test a large number of blades. Furthermore, historical methods for analysing these defects have relied on sequential sectioning and surface observations to identify their nucleating location and any relationship to the secondary/primary dendrite arm deflection. This method is inaccurate since appreciable coarsening of the secondary grain occurs, and they will obliquely intersect the observation plane. The stereology constraints makes this process both formidable and impractical for analysing a large population of defects efficiently. A better method is a crystallography based approach, where the  $\langle 001 \rangle$  directions from the SX and secondary grain can be accurately measured. Such methods have been adopted in the past, but with a focus on mosaicity.<sup>[6,7,34,35]</sup>

With consideration of the literature, this study aims to create a crystallographic based method to analyse a large population of castings with secondary grains to ascertain whether there is an associated deflection of the secondary/primary dendrites. Specifically, the strategy developed here can relate the spatial occurrence and misorientation of a secondary grain to the disposition of the primary grain orientation in the axial direction. The data will also describe whether a surface secondary grain has occurred when in contact with a converging or diverging mould wall. The unique set of measurements further permits the credibility of secondary grain formation theories, here argued to be governed by thermo-mechanical deformation, as well as future strategies for their unambiguous validation.

## II. EXPERIMENTAL METHODS

Blades from the 2nd generation Ni-base superalloy, CMSX4 were cast in a cluster mould using a directional solidification process, at a withdrawal rate of  $\sim 5 \times 10^{-5}$  m s<sup>-1</sup>. For full details of the casting method, the reader is referred elsewhere.<sup>[19]</sup> The shell constituting the ceramic mould comprises several layers and has a thickness of  $\sim 3$  to 5 mm. The prime coat in contact with the liquid metal is typically  $\sim 0.1$  to 0.8 mm thick and is composed of 18 wt pct colloidal silica (30 pct silica) and 82 pct zirconium silicate. The primary + 1 coat comprises 21 wt pct colloidal silica (25 pct silica) and 79 pct zirconium silicate. The remaining coats comprise 21 wt pct colloidal silica (38 pct silica) and 79 pct zirconium silicate.

Following solidification, the blades were given a solution heat treatment at  $\sim 1310$  °C for 6 hours to eliminate the as-cast micro-segregation and to dissolve any remnant non-equilibrium eutectic phases. A further ageing heat treatment at  $\sim 1140$  °C for 2 hours was then given. Thereafter, the blades were grit blasted to clean the surface and to remove any adhered mould shell. To reveal the grain structure, the blades were etched with FeCl<sub>3</sub> followed by an electro-etch with phosphoric acid. Figures 1(a) through (d) show some examples of secondary grains that can be seen on the root block and the aerofoil surfaces. Such images indicate a bias to their formation at the surface.

To facilitate a crystallographic analysis of secondary grain formation, seeded blades were studied, where both primary ( $\theta$ ) and azimuthal ( $\omega$ ) orientation control exists. The orientations of the three crystallographic basis vectors,  $\langle 001 \rangle$  are fixed with respect to the datum; this is fixed for the entire population of blades. This schematically illustrated in Figure 2, where the blade is viewed from the root to the shroud, resting on the convex face. Crystallographic measurements, both for the primary orientation with respect to the blade stacking axis (parallel to  $z$  in Figure 2) and the single crystal—secondary grain misorientation were measured using the Back-Reflection Laue method. Proto Laue Single-Crystal Orientation System, collecting X-ray data using a position and energy sensitive 2D camera. A dedicated

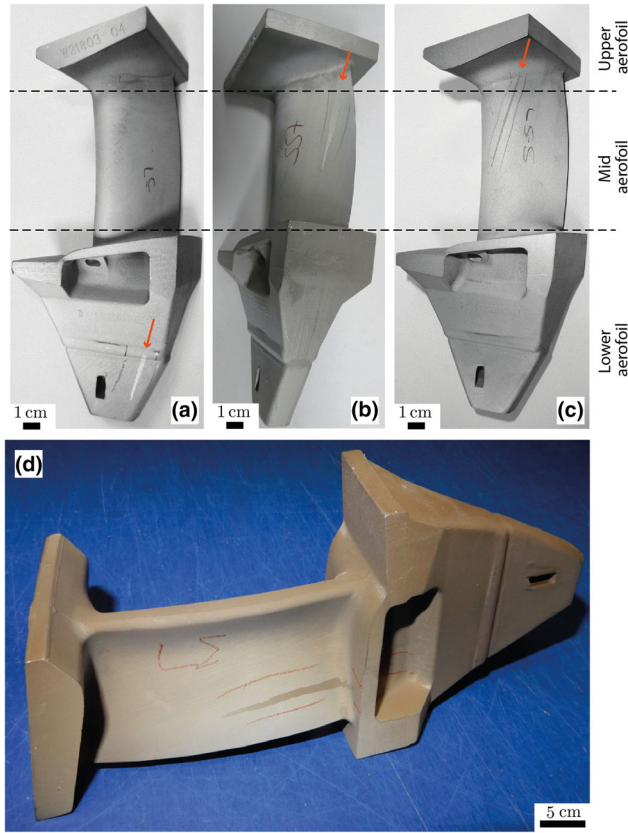


Fig. 1—Secondary grains, marked with arrows, observed on the external convex surface of a blade surface; examples shown at the (a) within to the root, (b) the convex face towards trailing edge, or (c) the convex aerofoil surface towards the leading edge. Also labelled are three horizontal sections along the height of the aerofoil; upper, mid and lower aerofoil. An example of secondary grains observed on a concave aerofoil surface is shown in (d).

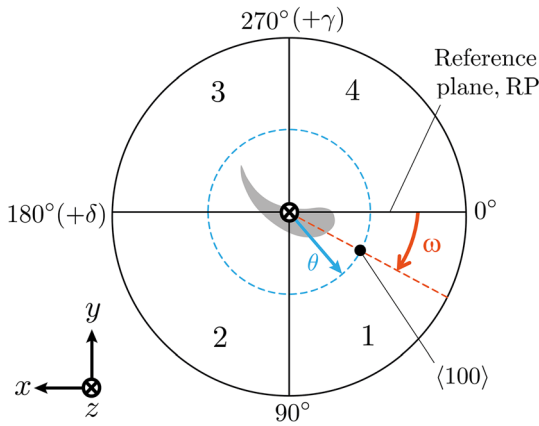


Fig. 2—Polar coordinate notation and reference Cartesian axes for the blade. The view here is from the bottom of the seed (root end of the turbine blade) (Color figure online).

fixture was used for aligning the blades during data collection. For the acquired diffraction patterns, data analysis and spot indexing was performed using an automated method. This provides the fundamental angles  $\gamma$ ,  $\delta$  and  $\alpha$  with respect to a fixed set of Cartesian

coordinate axes and a reference plane, as shown in Figure 2. For orientation, the accuracy is  $\pm 0.8$  deg for  $\gamma$  and  $\delta$  and  $\pm 1.0$  deg for  $\alpha$ . These angles are equivalent to the three Euler angles.<sup>[36]</sup> In the present case, both  $\gamma < 0$  and  $\delta < 0$ , are indicated in Figure 2. The axial orientation of the SX grain,  $\theta$ , is defined as the angle of a  $\langle 001 \rangle$  direction closest to the Z-axis. Here,  $\theta \approx 10.5$  to 17 deg for the population investigated. It follows that the azimuthal orientation range,  $\omega$ , is 35 to 45 deg.

Given the control on  $\theta$  and  $\omega$ , the spatial predilection of secondary grains occurrence can be obtained. From this, it can be found whether the primary  $\langle 001 \rangle$  SX directions are convergent or divergent to the external surface. Here, it is defects within the aerofoil that are of interest, as will be explored later. The aerofoil geometry is divided into three regions; nearest the root block, mid-aerofoil and nearest the shroud; the origin of the secondary grains can be broadly zoned into these three regions. This is done for convenience to investigate the occurrence of secondary grains along the length of the aerofoil and shown in Figure 1. Using the orientation descriptions shown in Figure 2, it is possible to obtain sections at fixed  $\omega \sim 40$  deg with respect to the reference plane (RP), as illustrated in Figure 3(a). Accordingly, the mid-aerofoil region can be split into regions where the primary  $\langle 001 \rangle$  dendrites of the SX converge or diverge across both the external as well as internal surface. To confirm this, longitudinal sections were taken across representative regions. The sections were prepared metallographically using abrasive media to a final polish of  $1/4 \mu\text{m}$  using a silica colloidal suspension. The sections were etched using nimonic. An example in the as-cast condition is shown in Figure 3(b); the dendritic structure is observable, magnified in Figures 3(c) and (d), as well as the orientation of the primary  $\langle 001 \rangle$  dendrites. It is noted that the observation plane contains both the blade stacking axis (Z-axis in Figure 2) and the primary  $\langle 001 \rangle$  dendrite, as manifested in the continuity of the stalks within this plane (with the orange dotted line in Figure 2).

To investigate any systematic misorientation relationships between the SX and the secondary grain, a formal coordinate transformation description between the crystals is necessary. This enables (1) a measure of the  $\langle 001 \rangle$  directions of the SX, and (2) an orientation measure of the secondary grain with respect to the external surface/SX reference axes. This is achieved by transforming the  $\langle 001 \rangle$  axes of the secondary grain onto the SX  $\langle 001 \rangle$  axes. The resulting transformation denotes the misorientation axis. Here, the approach in McCartney and Clay<sup>[37]</sup> is adopted:

$$\begin{aligned}
 [100] &= (\cos \delta \cos \kappa) \hat{i}_1 + (\cos \gamma \sin \kappa - \sin \gamma \sin \delta \cos \kappa) \hat{i}_2 \\
 &\quad - (\sin \gamma \sin \kappa + \cos \gamma \cos \delta \cos \kappa) \hat{i}_3 \\
 [010] &= -(\cos \delta \cos \kappa) \hat{i}_1 + (\cos \gamma \cos \kappa + \sin \gamma \sin \delta \sin \kappa) \hat{i}_2 \\
 &\quad - (\sin \gamma \cos \kappa - \cos \gamma \sin \delta \sin \kappa) \hat{i}_3 \\
 [001] &= (\sin \delta) \hat{i}_1 + (\sin \gamma \cos \delta) \hat{i}_2 + (\cos \gamma \cos \delta) \hat{i}_3
 \end{aligned} \tag{1}$$

where  $\hat{i}_1$ ,  $\hat{i}_2$  and  $\hat{i}_3$  define the reference axes, equivalent



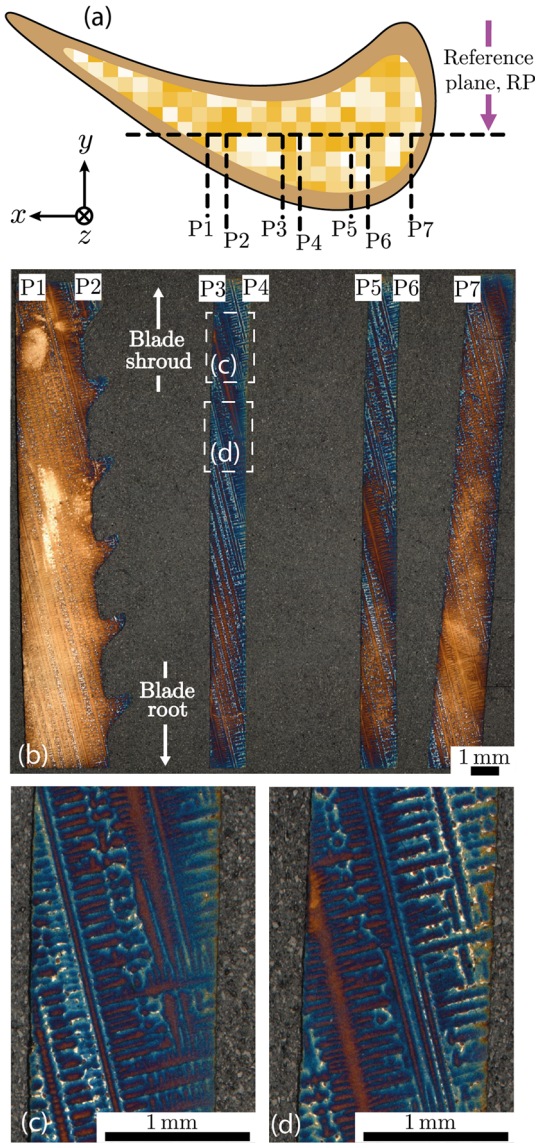


Fig. 3—(a) Cross section of the mid-aerofoil region with locations marked on internal sections. For proprietary reasons, details of the cooling passages are not shown. It is noted that the thickness of the metal ribs between successive cooling passages and the cooling passages nearest the surface to the external/internal surface is ~ 1 to 2 mm. The  $X$ ,  $Y$  and  $Z$  axes are as indicated. Observing along the reference plane, (b), the orientation of the  $\langle 001 \rangle$  primary dendrites with respect to the blade geometry is shown. The dendrites at a higher magnification are shown in (c) and (d).

to the axes  $x$ ,  $y$  and  $z$  in Figure 2. Note that these axes are fixed with respect to the macroscopic blade geometry. The directions  $\langle 001 \rangle$  define the basis vectors for the measured SX or secondary grain. The angle  $\kappa$  is calculated *via* Eq. [2]

$$\tan \kappa = \frac{\tan \alpha \cos \gamma}{\cos \delta - \tan \alpha \sin \gamma \sin \delta} \quad [2]$$

where  $\alpha$  is calculated from:

$$y = x \tan \alpha \quad [3]$$

In Eq. [3],  $x$  and  $y$  are measured coordinates along the

reference vectors  $\hat{t}_1$  and  $\hat{t}_2$ , respectively. Equation [1] can be represented in matrix notation as:

$$\begin{bmatrix} 1 & 0 & 0 \\ 0 & 1 & 0 \\ 0 & 0 & 1 \end{bmatrix} = \mathbf{M} \begin{bmatrix} x \\ y \\ z \end{bmatrix} \quad [4]$$

where  $\mathbf{M}$  is a  $3 \times 3$  rotation matrix whose elements are found from Eq. [1].

The misorientation matrix between the SX and a secondary grain is therefore given by  $\mathbf{M} = \mathbf{M}_{\text{SX}} \mathbf{M}_{\text{Sec}}^{-1}$  or  $\mathbf{M} = \mathbf{M}_{\text{Sec}} \mathbf{M}_{\text{SX}}^{-1}$ , where  $\mathbf{M}_{\text{SX}}$  and  $\mathbf{M}_{\text{Sec}}$  are the individual rotation matrices of the SX and the secondary grain. Due to symmetry there are 24 equivalent solutions,  $\Phi/[hkl]$ , where  $\Phi$  is the misorientation angle and  $[hkl]$  is the misorientation axis.<sup>[36]</sup> While the rotation matrix for the SX can be obtained using Eqs. [1] through [4], the secondary grain in the reference frame of the SX is;

$$\langle 001 \rangle_{\text{SX}} = \mathbf{M}_{\text{SX}} \langle \mathbf{x} \rangle \quad [5]$$

$$\langle 001 \rangle_{\text{Sec}} = \mathbf{M}_{\text{Sec}} \langle \mathbf{x} \rangle \quad [6]$$

where  $\langle 001 \rangle$  and  $\langle \mathbf{x} \rangle$  are both  $3 \times 1$  vectors, as in Eq. [4], however, the reference system is arbitrary. From Eqs. [5] and [6];

$$\langle 001 \rangle_{\text{Sec}} = \mathbf{M}_{\text{Sec}} \mathbf{M}_{\text{SX}}^{-1} \langle 001 \rangle_{\text{SX}} \quad [7]$$

However, from Eq. [4] with respect to the blade reference axes;

$$\langle 001 \rangle_{\text{SX}} = \mathbf{M}_{\text{Rot,SX}} \langle \mathbf{x} \rangle \quad [8]$$

where  $\langle \mathbf{x} \rangle$  is the datum for the SX. From Eqs. [7] and [8];

$$\langle 001 \rangle_{\text{Sec}} = \mathbf{M}_{\text{Sec}} \mathbf{M}_{\text{SX}}^{-1} \mathbf{M}_{\text{Rot,SX}} \langle \mathbf{x} \rangle \quad [9]$$

where the  $3 \times 3$  matrix,  $\mathbf{M}_{\text{Sec}} \mathbf{M}_{\text{SX}}^{-1} \mathbf{M}_{\text{Rot,SX}}$  gives the direction cosines of the  $\langle 001 \rangle$  axes of the secondary grain with respect to the same datum as the SX.

The misorientation axis,  $[hkl]$ , is found from the elements,  $M_{ij}$ , of the misorientation matrix,  $\mathbf{M}$ , by;

$$[hkl] = (M_{32}M_{23}) (M_{13}M_{31}) (M_{21}M_{12}) \quad [10]$$

Equation [10] has equal angles to the three crystal axes;  $\langle 001 \rangle$  of the secondary and SX.<sup>[36]</sup> Therefore  $[hkl]$  is defined with respect to  $[100]$ ,  $[010]$  and  $[001]$  of either the secondary grain or SX. The misorientation axis vector in the datum for the SX is given by;

$$[hkl] \cdot \langle 001 \rangle_{\text{SX}} = [hkl] \cdot \mathbf{M}_{\text{Rot,SX}} \langle \mathbf{x} \rangle, \quad [11]$$

where  $[hkl]$  is a  $1 \times 3$  vector,  $\langle 001 \rangle_{\text{Sec}}$  is a  $3 \times 1$  vector,  $\mathbf{M}_{\text{Rot,SX}}$  is a  $3 \times 3$  matrix and  $\langle \mathbf{x} \rangle$  is a  $3 \times 1$  vector.

Of importance to this study is the disposition determination of the secondary grain  $\langle 001 \rangle$  directions in the same coordinate system as the SX, *i.e.*,  $\mathbf{M}_{\text{Rot,Sec}} \langle \mathbf{x} \rangle$ , which is not directly obtained from Laue measurements. The disposition of the  $\langle 001 \rangle$  directions for the SX is known in the blade reference system, as in Figure 2, as

$M_{\text{Rot,Sec}}(\mathbf{x})$  in Eq. [8] is obtained from Eqs. [1] through [3]. The only way to obtain  $M_{\text{Rot,Sec}}(\mathbf{x})$  is indirectly *via* Eq. [9], combining Eqs. [5], [6] and [8] to obtain the disposition of the  $\langle 001 \rangle$  directions for the secondary grain in the SX reference frame.

### III. RESULTS

#### A. Spatial Classification of Secondary Grains and Relation to Primary Dendrite Inclination

The location of a secondary grain within a turbine blade is random, however, they are always located at/near the proximity of the external surface. Some typical examples are shown in Figures 1(a) through (d), where the blade has been etched following heat treatment. The visible contrast of the grains after etching arises from the differential reflection of light from crystals of different orientations. The misorientation angle of the secondary grains with respect to the SX grain are reported in Figure 4.

The misorientation of 82 grains are within a maximum of 16 deg and 5 grains that exceed 19 deg. Of the latter, three samples possessed a misorientation exceeding 25 deg. Considering most cases are low angle, an orientation relationship must exist between the SX and the secondary grain; the following analysis considers these. Since the primary  $\langle 001 \rangle$  orientation of the SX grain is off-axial, the primary  $\langle 001 \rangle$  dendrites can have either a converging or diverging disposition with the external surface. The aim is to determine if the spatial origin of a secondary grain shows a bias to a converging or diverging disposition. A simplification is made to consider only a region along the blade length where the cross-section is approximately constant and any taper along the length is minimal.

Figures 5(a) through (d) schematically illustrates views of the turbine blade. The aerofoil region has both concave (CC) and convex (CV) surfaces with two edges; leading edge (LE) and trailing edge (TE). Three positions are considered along the length of the aerofoil, *i.e.*,

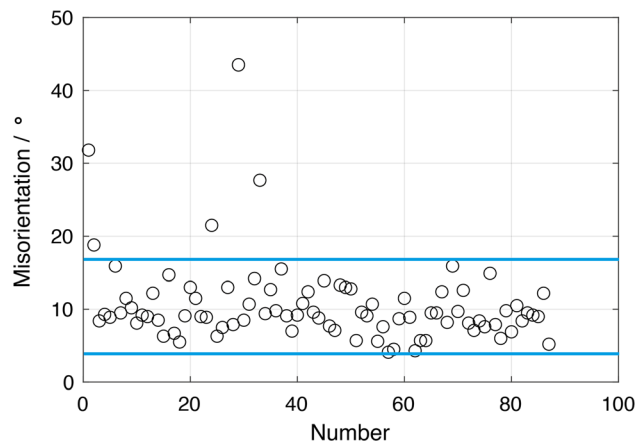


Fig. 4—Misorientation of the secondary grain with respect to the single crystal, measured for 87 samples. The datapoints within the blue lines are considered as low angle (Color figure online).

close to the root platform, mid-aerofoil and upper aerofoil section closest to the shroud. The origin of the secondary grains originating within the aerofoil can be broadly classed into these three regions, as in Figures 6(a) through (c) respectively. It is observed that (1) secondary grains have a greater propensity to originate on aerofoil sections either close to the root platform or the shroud. Also, (2) secondary grains originate at both the converging and diverging dispositions, with a slight bias to the latter. Finally, (3) at the aerofoil root there is a marked population of secondary grains at the diverging condition (CV-LE), while nearer the shroud most secondary grains occur at the diverging condition (CC-TE) or converging case (CC-LE). Note that cases of divergent and converging are labelled as D and C, respectively, in Figure 6.

The location clustering of the secondary grain population in Figures 6(a) through (c) indicates a strong geometry effect for their formation. This is further supplemented by the crystallographic analysis that calculates the disposition of the primary SX grain with the surface. This additional attribute is one advantages of the approach presented here. From Figures 6(a) through (c), it is concluded that the predilection for the secondary grains origins are:

1. *Lower* aerofoil closest to the root: diverging (CV-LE) and Converging (CC-LE).
2. *Mid*-aerofoil: diverging (CC-TE).
3. *Upper* aerofoil closest to the shroud: diverging (CV-LE) and Converging (CC-TE).

From the population examined, secondary grains are most likely at the *Lower* aerofoil closest to the root—diverging (CV-LE) and the *Upper* aerofoil closest to shroud—converging (CC-TE). Whilst a larger dataset is necessary to make a more definitive statement, the experimental evidence here is sufficient to examine existing theories proposed for secondary grains formation.

#### B. Detailed Crystallographic Analysis of Secondary Grains

The misorientation data presented in Figure 4 warrants a more in-depth analysis. To do this, the angular representation of  $[100]$ ,  $[010]$  and  $[001]$  of both the SX grain and secondary grain in the Cartesian coordinate system of the blade datum is required. Following the approach in Section II, some representative cases are presented on stereograms in Figures 7(a) through (f); the  $\langle 001 \rangle$  poles of the secondary grain and SX are plotted. These examples, representative of the entire population, show the primary  $\langle 001 \rangle$  diverges from the external surface. It is observed that the rotation of the three  $\langle 001 \rangle$  poles of the secondary grain with respect to the SX grain is random and not systematic.

Since the stability (competitive growth) of the secondary grain with respect to the primary SX is determined by their axial orientations ( $\theta$  in Section II), these

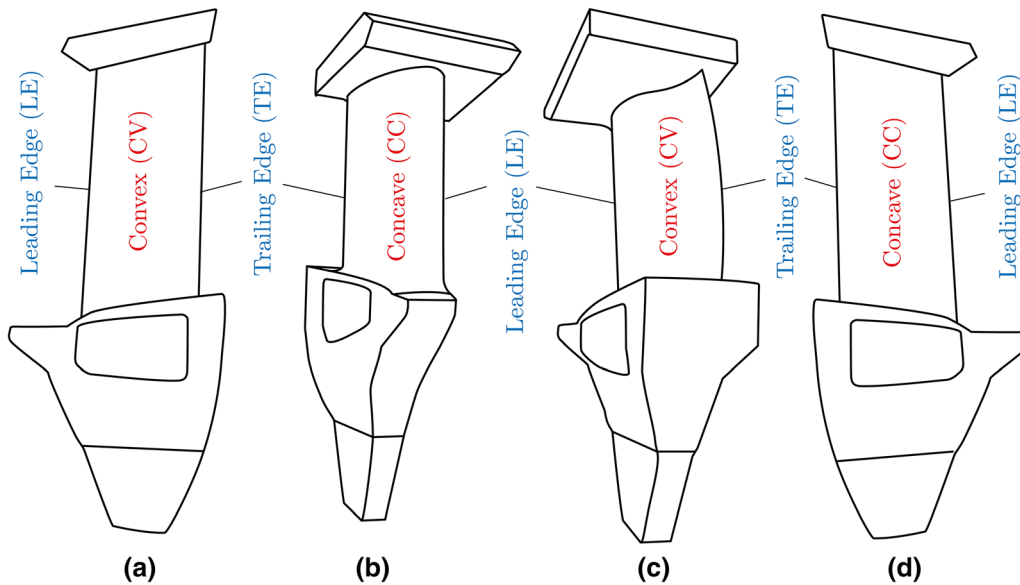


Fig. 5—Different views of the turbine blade with key geometric features labelled.

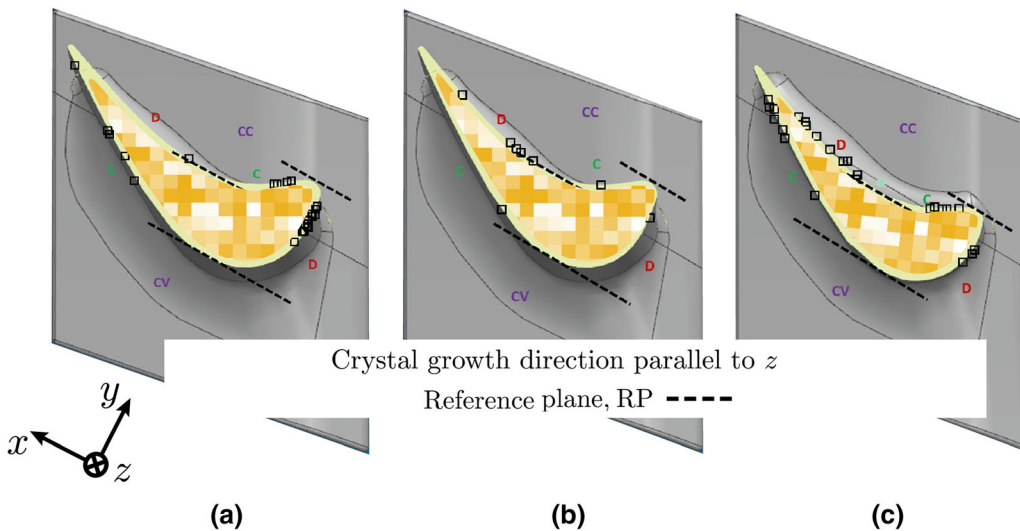


Fig. 6—Aerofoil cross sections across three example blades (a), (b) and (c), with identified locations of secondary grains, each marked with a black square. Labels around the aerofoil are given, where ‘CC’ is concave, ‘CV’ is convex, ‘C’ is convergent and ‘D’ is divergent. For proprietary reasons, details of the cooling passages are not shown.

are individually plotted for the entire dataset in Figure 8(a). A direct comparison between the secondary grain and the SX is made in Figure 8(b) to ascertain whether any trend exists. No marked trend is evident in the axial orientation of the secondary grains with respect to the SX grain. There is a wide range of  $\langle 001 \rangle$  secondary grain directions which can form with either lower or greater axial orientations, in relation to the SX. There is, however, a small bias towards an increasing axial orientation for the secondary grains.

The misorientation accounts for deviation of the individual  $\langle 001 \rangle$  directions between the SX and the secondary grain, and not just the deviation in the axial orientation shown in Figures 8(a) and (b). Accordingly, in Figures 9(a) through (c), the deviation of the  $[100]$ ,

$[010]$  and  $[001]$  directions between the secondary grain and SX are presented, respectively, for the diverging disposition of the primary orientation, *i.e.*, a  $[001]$  direction with the external surface (CV-LE and CC-TE). In a similar fashion, Figures 9(d) through (f) these directions are plotted for the converging case (CV-TE and CC-LE). The misorientations are also included. For completeness, the angular measurements are given in Table I for both the diverging and converging cases.

It is observed that the deviations between the  $[100]$ ,  $[010]$  and  $[001]$  SX and the secondary grain directions are less than or equal to the misorientation. This supports the proposed existence of low angle boundaries. Furthermore, the misorientation comprises a tilt as well as twist contribution. The bias for twist can be



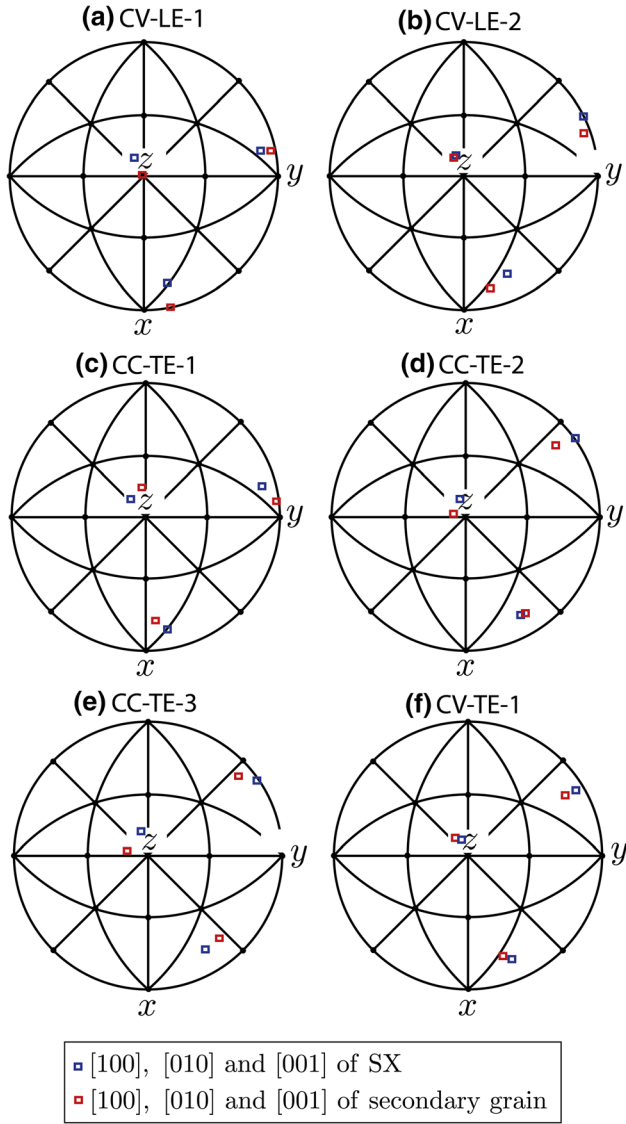


Fig. 7—Stereogram representation of the  $\langle 001 \rangle$  directions for both the primary crystal, SX, and secondary grains with respect to the macroscopic blade axes,  $x$ ,  $y$  and  $z$ .

deduced by comparing Figures 9(a) through (c) (diverging) with Figures 9(d) through (f) (converging). There is a larger population of secondary grains in the converging case (8 out of 15), where a small orientation deviation of the secondary arms with respect to the primary occurs, as highlighted by the blue dashes in Figures 9(d) and (e). This indicates a twist about an axis close to the  $[0\ 0\ 1]$  of the primary arm. This is schematically shown in the stereogram in Figure 7(f). For the case of the diverging  $\langle 001 \rangle$  from the external surface in Figures 9(a) through (c), the secondary grains generally have a deviation in all of their  $\langle 001 \rangle$  axes with respect to the SX grain, *i.e.*, deviations exist between each of the individual  $[1\ 0\ 0]$ ,  $[0\ 1\ 0]$  and  $[0\ 0\ 1]$  of the secondary grain and SX. This indicates a tilt and twist contribution to the misorientation.

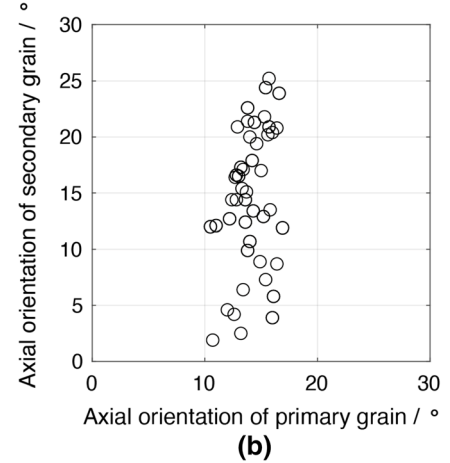
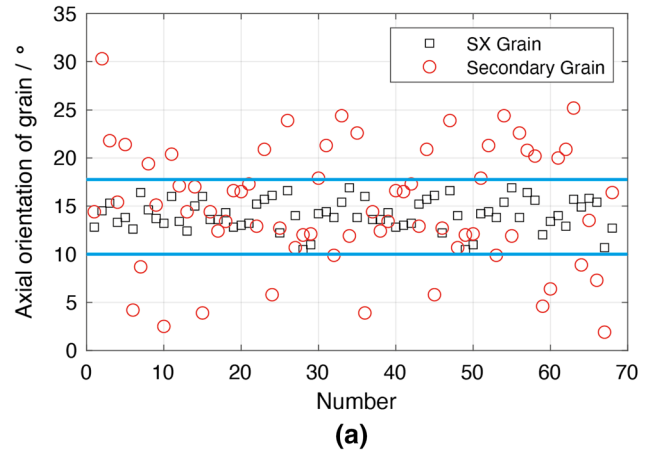


Fig. 8—(a) Axial orientation spread of the population of SX grains and (b) plot of the axial orientation of secondary grain with primary (SX) grain.

This can be better visualised when the misorientation axis is represented in a stereogram, as shown in Figures 10(a) through (h). Also plotted is the orientation of the closest secondary arm of the SX. The reference axes is that of the blade, as in Figures 7(a) through (f). It is observed that the misorientation axis,  $\langle hkl \rangle$ , lies within  $\sim 30$  deg of the secondary arm orientation (for the cases shown Figures 10(g) and (h), this is deduced from the  $\langle -h - k - l \rangle$  pole).

## IV. DISCUSSION

### A. Critical Assessment of Theories for Secondary Grain Formation

The nucleation of a secondary grain is linked to undercooling. Typical values of undercooling in Ni-base alloys, as measured from calorimetry, is  $\sim 5$  K.<sup>[38]</sup> In directional solidification, where a positive thermal gradient exists, nucleation, if at all possible, must occur either in the constitutionally undercooled layer just ahead of the primary tips or behind the dendrite tips, within the inter-dendritic grooves. The extent of solutal undercooling behind the primary dendrite tips is

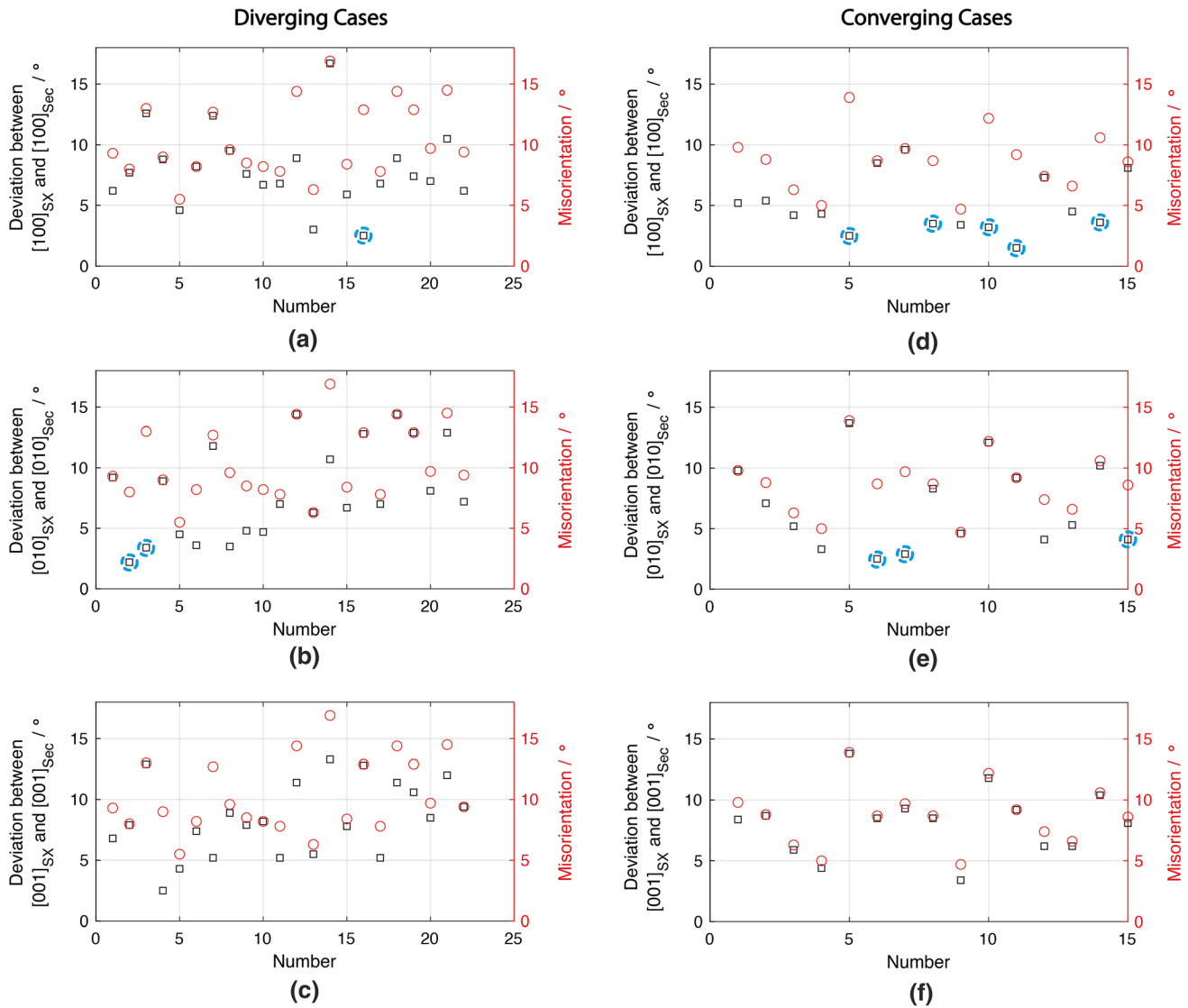


Fig. 9—Black squares represent the deviation between the  $[1\ 0\ 0]$  of the primary grain and secondary grain, deviation between the  $[0\ 1\ 0]$  of the primary grain and secondary grain and deviation between the  $[0\ 0\ 1]$  of the primary grain and secondary grain. Red circles represent the corresponding misorientation (Color figure online).

dependent on the primary dendrite arm spacing and the development of secondary dendrite arms. For a smaller arm spacing with a greater number of secondary arms, the solutal undercooling is lowered. When above a critical solid fraction, the undercooling becomes negligible and solidification is then governed by back-diffusion in the solid.<sup>[39,40]</sup> If the solutal undercooling exceeds the nucleation undercooling, then nucleation of a secondary grain occurs. If the presence of impurities or oxide bi-films engenders such heterogeneous nucleation, as suggested in References 29 and 30, then there should be a complete absence of any orientation relationship between the secondary grain and the substrate (in this case, the SX). However, such an analysis is noticeably missing with no reports of measured misorientation. Furthermore, the misorientation distribution should be similar to the Mackenzie plot, which has been experimentally verified for random

grain nucleation in the chill zone of a casting.<sup>[41,42]</sup> Notably, the misorientation distribution in Figure 4 is at complete variance to the Mackenzie plot. As the axial orientation of the secondary grains are mainly within  $\sim 17$  deg off- $\langle 001 \rangle$ , Figure 4, the magnitudes could be compared to those seen in the misorientation distribution, as texture develops, during competitive grain growth.<sup>[42]</sup> For this case the comparison is poor as there exists a large population of misorientations beyond  $\sim 17$  deg in the presence of texture, but is noticeably absent in Figure 4. It is therefore unequivocally concluded that nucleation must be precluded as a mechanism for the formation of secondary grains.

From the analysis in Section IV-A, it is concluded that nucleation from inclusions or say Pt pins added to hold the ceramic core in place during the wax injections stage, as a mechanism can be ruled out, since an orientation relationship exists between the secondary



**Table I. Misorientation (Mis.) and Deviation of  $\langle 001 \rangle$  Directions of the Secondary Grain to the SX When a Primary  $\langle 001 \rangle$  Direction of the SX Diverges (CV-LE-1 to CV-LE-10 in 1st Block and CC-TE-1 to CC-TE-10 in 2nd Block) and Converges (CV-TE-1 to CV-TE-8 in 3rd Block and CC-LE-1 to CC-LE-7 in 4th Block) at the External Surface**

Identifier	Mis./((deg)	[1 0 0]/((deg)	[0 1 0]/((deg)	[0 0 1]/((deg)
*CV-LE-1	13	12.6	3.4	12.9
CV-LE-2	9	8.8	8.9	2.5
CV-LE-3	5.5	4.6	4.5	4.3
CV-LE-4	8.2	8.2	3.6	7.4
CV-LE-5	12.7	12.4	11.8	5.2
CV-LE-6	9.6	9.5	3.5	8.9
CV-LE-7	8.5	7.6	4.8	7.9
CV-LE-8	8.2	6.7	4.7	8.2
CV-LE-9	9.3	6.2	9.2	6.8
CV-LE-10	8	7.7	2.2	7.9
CC-TE-1	8.4	5.9	6.7	7.8
CC-TE-2	12.9	2.5	12.8	12.8
CC-TE-3	14.4	8.9	14.4	11.4
CC-TE-4	12.9	7.4	12.9	10.6
CC-TE-5	9.7	7	8.1	8.5
CC-TE-6	14.5	10.5	12.9	12
CC-TE-7	9.4	6.2	7.2	9.4
CC-TE-8	7.8	6.8	7	5.2
CC-TE-9	6.3	3	6.3	5.5
CC-TE-10	16.9	16.7	10.7	13.3
CV-TE-1	8.8	5.4	7.1	8.7
CV-TE-2	13.9	2.5	13.7	13.8
CV-TE-3	8.7	3.5	8.3	8.5
CV-TE-4	8.7	8.5	2.5	8.5
CV-TE-5	9.7	9.6	2.9	9.3
CV-TE-6	9.8	5.2	9.8	8.4
CV-TE-7	6.3	4.2	5.2	5.9
CV-TE-8	5	4.3	3.3	4.4
CC-LE-1	12.2	3.2	12.1	11.8
CC-LE-2	9.2	1.5	9.2	9.2
CC-LE-3	10.6	3.6	10.2	10.4
CC-LE-4	8.6	8.1	4.1	8.1
CC-LE-5	7.4	7.3	4.1	6.2
CC-LE-6	6.6	4.5	5.3	6.2
CC-LE-7	4.7	3.4	4.6	3.4

The identifier denotes the positions, CV (convex aerofoil surface), CC (concave aerofoil surface), LE (leading edge) and TE (trailing edge) with the sample number. Those denoted with (\*) are plotted in the stereograms shown in Figs. 7 and 10.

grain and the SX grain, as in Figures 4, 8 and 9(a) through (f). With regards the Pt pins, these are only located at certain regions of the aerofoil, but there is no relationship of the spatial locations of the secondary grains at these locations. Moreover, secondary grains are also observed in the root block, where no pins exist. One of the principal conclusions is that the secondary grains have their origin with the SX grain and arise from tilt/twist about certain axes, as in Figure 10, which have some relation to the  $\langle 001 \rangle$  axes of the SX grain.

Buoyancy driven thermo-solutal convection also plays a role in dendrite fragmentation, but this is mainly through re-melting at the secondary dendrite root.<sup>[11]</sup> Fragmentation from mechanical stresses (shear and hydrostatic) arising from the interaction of the secondary arms with the solute plumes has been argued to be impossible.<sup>[43]</sup> However, three reasons militate against such an operating mechanism being possible;

- (a) Convection occurs only when a steep curvatures exist in the liquidus isotherms that reduce the

inertial forces that retard the plumes. Such steep curvatures are absent in narrow cross-sections like in aerofoils with a typical metal thickness of 1.5 to 2 mm. This is because a predominantly axial thermal flux exists with a minimal radial contribution. Importantly for stabilising these convection channels, an entrainment volume is required. The channel widths are at least three primary dendrite arm spacings or  $\sim 1$  mm, which is almost the thickness of the metal in the aerofoil and therefore insufficient liquid exists to support an entrainment volume.<sup>[11]</sup>

- (b) Such dendrite fragments are either advected into the bulk liquid or sink into the mush, depending on their size. In the latter, the grain will be equiaxed, while in the former, if it manages to grow in an undercooled liquid, it will eventually be captured by the advancing solid and will form a high angle boundary with the SX. Both of these

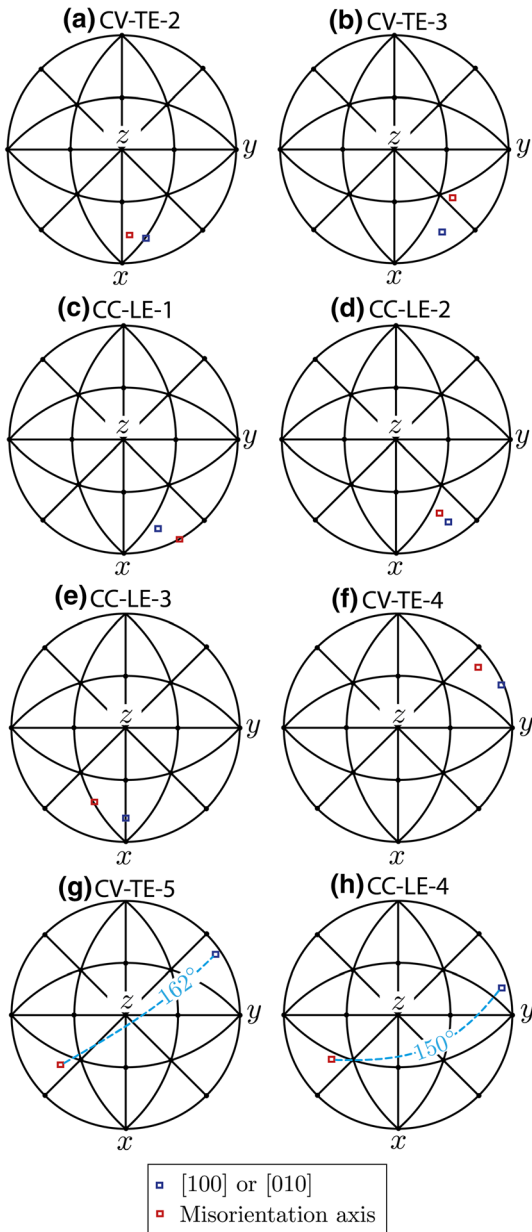


Fig. 10—Stereogram representation of the misorientation axis, between the SX and the secondary grain. The [100] or [010] direction, whichever is closest to the misorientation axis, of the secondary arms is also plotted.

characteristics are not observed in the secondary grains, as in Figure 4.

- (c) The existence of solute plumes leads to macro-segregation that cannot be eliminated through heat treatment, owing to length-scales. These channels with eutectic-rich solute will etch with a distinctive contrast compared to the matrix; this is clearly absent in the region of the secondary grains, as in Figures 1(a) through (d).

Consequently, the role of thermo-solutal convection must also be excluded as a possible mechanism.

## B. Contribution from Thermo-Mechanical Deformation

The locations of the forming secondary grains in Figures 6(a) through (c) indicates that the blade geometry must be influential. Thermo-solutal convection is dictated by the curvature of the liquidus isotherms, which in turn is dependent on the thermal mass and hence the geometry effect. However, from point (c) in Section IV-A, the absence of macro-segregation solute trails rules out the role of thermo-solutal convection conclusively. This indicates the role of thermo-mechanical deformation of the solid, which is also location-specific, as it is dependent on the local cooling rate and hence determines the accumulation of plastic strain. Therefore, following from Section IV-A, the most likely origin for secondary grain formation during directional solidification is related to thermo-mechanical deformation of the dendrites. However, unlike in Reference 44 where the deformation occurs at a high solid fraction when the dendrites have bridged and long-range stresses can be transmitted, in the present case deformation must occur close to the dendrite tips. It can be deduced that a secondary grain origin must occur in close proximity to the primary dendrite tips, since the  $\langle 001 \rangle$  dendrites of the secondary grain must compete with those of the SX grain, else they will be unable to grow and will remain equiaxed. This is precisely what happens in the case of freckles, where the dendrite fragments (unless advected into the bulk liquid through the solute plumes) sink (heavier) into the inter-dendritic region and are quickly overgrown by the engulfing solid mush of the SX grain. The origin of any secondary grains must occur in close proximity to the primary dendrite tips, such that the primary dendrites of the secondary grain will grow competitively with those of the SX. The deformation at near liquidus temperatures indicates the prominence of viscoplasticity, which has been shown to be dominant above the solvus temperature in Ni-base alloys.<sup>[45,46]</sup> Body forces producing a torque, as will occur in a cantilever beam, has been proposed to cause dendrite bending. This has been supported by experimental evidence.<sup>[18–20,22–24]</sup> The following considerations are, however, important:

- Condition 1: A bending dendrite must be oriented at an angle greater than 45 deg to the gravity vector.
- Condition 2: For bending to prevail under body forces, the bending dendrites must have not bridged and remain isolated from the neighbouring solid. If the solid has bridged to a limited degree, then the extent to which the solid skeleton can resist bending is dictated by the strength of the network and plasticity of the solid. Both considerations favour bending closer to the primary dendrite tips. This is because the secondary arms are less branched and therefore solid bridging is limited; the solid is characterized by significant plasticity.

To ensure that dendrites have not bridged, the primary arm growth direction must be significantly inclined to the gravity vector (horizontal solidification), as in References 22–24. Bridging is similarly avoided if a discontinuity exists in the cross-section, such as a platform, where a secondary arm grows into an increasing volume of undercooled liquid.<sup>[18–20]</sup> In both cases, bridging occurs between the secondary or tertiary arms respectively at a much higher solid fraction, by which time bending would have already occurred.

Condition 1 is most favourably met only by secondary arms when the solid is growing near-parallel to the gravity vector. At the diverging end, for a tertiary arm emanating from the bent secondary (from body forces, *i.e.*, Condition 2) to escape the solute field of the parent primary arm/adjacent secondary arms, the “parent” bent secondary arm must grow a sufficient length before reaching the external surface, as in Figure 3(b). There is uncertainty in determining this length, since coarsening has also occurred and the plane of observation can intersect the arm obliquely. However, from Figure 3(b) a reasonable estimate of this characteristic length of the secondary arm is at least  $\sim 0.75$  to 1 mm, such that the tertiary dendrite arms can escape the solute field and grow. However, body forces alone cannot account for the predilection of the secondary grains to the external surface. This is because branching of secondary dendrite arms always occurs across the cross-section and not just at the surface. The bias of the secondary grains to the external surface clearly points to an interaction of the secondary dendrites with the external mould wall. For a force between the tip of the secondary arm and the mould wall, cantilever type bending can be envisaged. Deformation will be focused at the small radius of curvature where the secondary arm is joined to the primary. Using the thin-beam flexure equations<sup>[47]</sup>,

$$\delta_{\text{Max}} = \frac{PL^3}{3EI} \quad [12]$$

$$\sigma = \frac{PLy}{I}, \quad [13]$$

where  $\delta_{\text{Max}}$  is the maximum displacement from the applied force,  $P$ ,  $L$  is the beam length of,  $E$  is the elastic modulus,  $I$  is the second moment of area and  $y$  is the distance from the neutral axis. Further, for small misorientations, as in the case for the secondary grains in Figure 4;

$$\tan R' \approx \frac{\delta_{\text{Max}}}{L}, \quad [14]$$

where  $R'$  is the misorientation angle due to elastic deformation. Using the approximation that  $\sigma = E \cdot 1 \times 10^{-3}$  (0.1 pct elastic strain), this term is redefined;

$$\tan R' \approx \frac{1}{1000} \frac{L}{3y} \quad [15]$$

From Figure 3(b), the approximate length of the secondary arm, such that tertiary arms emanating from it can escape the solute field from the secondary arms above it and also the primary tip is  $\sim 0.5$  to 1 mm. A possible range exists, since there is some error in deducing this from micrographs, where the secondary arms will obliquely intersect the observation plane. Interestingly, this compares well with numerical simulations using a binary system in Reference 48, where a similar range in average primary dendrite arm spacing of  $\sim 400$  to  $450 \mu\text{m}$  is reported. The typical thickness of the secondary arms measured from Figure 3(b) will contain a contribution of coarsening. Following from the similarity in the length of the secondary arm intersecting the surface at the diverging end between simulation and experiment, a characteristic thickness of the  $\sim 25$  to  $50 \mu\text{m}$  can be taken at the instance when the secondary arm abuts the surface. From Eq. [15], this gives,  $R' \approx 0.38$  to  $0.76$  deg. This is nearly 50 times smaller than the measured misorientation. This is to be expected, since the deflection will be accommodated almost exclusively through creep plasticity in these conditions.<sup>[45]</sup> Therefore, an elastic analysis, as in Reference 22 will significantly underestimate the misorientation at temperatures close to the liquidus.

The character of the secondary arms is mostly relevant at the diverging disposition, *i.e.*, Figures 3(d) and (e) and quantitatively described through Eqs. [12] through [15]. If a secondary arm bends when interacting with the mould wall, then the emanating tertiary arms will compete with the solute field of the primary and other secondary arms of the abutting SX grain. With increasing distance behind a leading  $\langle 001 \rangle$  direction of the SX grain, the tertiary arm from the bent secondary arm will grow less competitively with the SX grain and will be easily overgrown.

### C. Influence of the Primary Dendrite Orientation Surface Interactions

While the deflection of secondary dendrite arms at the external surface can be understood, the occurrence of secondary grains at the converging disposition presents features of interest, since the primary arms abut the surface. A key insight can be gained by comparing Figures 9(a) through (c) with Figures 9(d) through (f) and Figures 10(a) through (h). While in the converging case a significant proportion of twist about one of the secondary arms contributes to the overall misorientation (half of the population), only  $\sim 15$  pct of the diverging population shows this. Tilt increasingly prevails in this case. A specific micromechanism to account for this bias of twist is out of the scope of this paper, but a key difference is evident in the nature of the misorientation that develops when the primary SX  $\langle 001 \rangle$  dendrites converge or diverge from the external surface.

The requirement for an external force at the mould surface that exceeds the body force has been identified for the diverging case in the preceding section, but is more significant at the converging end as the primary dendrites encounter deflection. It has been proposed in References 26 and 27 that a radial (perpendicular to the



axial thermal gradient or growth direction) force will develop owing to the differential contraction between the ceramic mould and the metal during cooling. A similar case will also result at the internal ceramic core/metal interface. However, such forces will only occur at a large fraction solid ( $f_s > 0.75$ ), when dendrites have bridged (coherency and rigidity temperatures) and long-range stresses can be transmitted.<sup>[49,50]</sup> It has been shown that in the present case, the origin of secondary grains must occur in the vicinity of the primary tip, making this argument invalid. A key feature of directional solidification is the axial heat flux at the solid/liquid interface, resulting in an axial thermal strain. During axial contraction, for any secondary/primary stems where the interface intersects the external surface, resistance will be present. The forces here will most certainly lead to deflection and misorientation owing to the extreme ductility at these temperatures.<sup>[45]</sup> The interfacial resistance will arise primarily from the intrinsic roughness of the mould prime coat in contact with the metal. The topography of this surface can also be modified by the oxides formed during mould-metal reactions.<sup>[51-53]</sup> It follows that the nature of the mould prime coat and its interaction with the dendrite tips close to the liquidus temperature, as well as the strength and ductility of the solid at such temperatures, are key controlling parameters. These areas should be investigated in context to mechanisms for secondary grain formation.

The role of competitive growth of the secondary grain in relation to the primary grain plays a pivotal role in its stability. For randomly orientated stray grains (nucleating at the melt-back interface of a SX seed), only those with a diverging disposition from the SX prevail.<sup>[48,54,55]</sup> In this study this is not observed; secondary grains at both the converging and diverging disposition are equally prominent.

## V. CONCLUSIONS

A large population of secondary grains of statistical significance has been investigated in directionally solidified Ni-base superalloy, CMSX4 turbine blades. This has permitted a mechanism for the formation of these defect to be identified with the following key conclusions:

1. All secondary grains originate exclusively at the external surface. Secondary grains occur at both the converging and diverging dispositions of the primary  $\langle 001 \rangle$  SX dendrites with the external surface.
2. Almost all of the secondary grains (83 out of 87 tested) have misorientations within 20 deg, having an average misorientation between 5 to 15 deg. The deviation between the individual  $\langle 001 \rangle$  directions of the secondary grain and the SX along with the low overall misorientation possess a clear orientation relationship between the crystals, eliminating nucleation as a potential mechanism.
3. The absence of enriched solute channels with narrow metal features within the aerofoil cannot

contain an entrainment volume. The non-random misorientation of secondary grains with respect to the SX also eliminates thermo-solutal convection as a nucleation mechanism.

4. Thermo-mechanical deformation is the most likely cause for the origin of secondary grains. From the stabilisation of secondary grains, deformation originates in the vicinity of the dendrite tips. The force causing deflection of the dendrite stem must arise from the resistance encountered by the primary tips with the external surface during axial contraction in the presence of a dominant axial thermal gradient.
5. No systematic deviation between the individual  $\langle 001 \rangle$  directions of the secondary grain and the SX is observed. A significant twist contribution about an axis within  $\sim 30$  deg from one of the secondary dendrite arms occurs for convergent cases. This condition corresponds to the primary dendrite arms intersection with the external surface. For diverging cases, both twist and tilt of the misorientation axis prevails.
6. This study highlights the necessary consideration of the mould/metal topography, roughness and interfacial reactions during solidification, with their influence on a forming secondary grain dependent on the crystallographic directions of the growing crystals. The analysis indicates that undercooling and nucleation only plays a marginal role in the formation of secondary grains.

## ACKNOWLEDGMENTS

The assistance of Matthew Conlin in metallography, Dr. Graham Bing for assistance in CAD sections to generate the secondary grain meale plots and Chris Byrne is Laue measurements is gratefully acknowledged.

## CONFLICT OF INTEREST

The authors declare that they have no conflict of interest.

## OPEN ACCESS

This article is licensed under a Creative Commons Attribution 4.0 International License, which permits use, sharing, adaptation, distribution and reproduction in any medium or format, as long as you give appropriate credit to the original author(s) and the source, provide a link to the Creative Commons licence, and indicate if changes were made. The images or other third party material in this article are included in the article's Creative Commons licence, unless indicated otherwise in a credit line to the material. If material is not included in the article's Creative Commons licence and your intended use is not permitted by statutory regulation or exceeds the permitted use, you will need

to obtain permission directly from the copyright holder. To view a copy of this licence, visit <http://creativecommons.org/licenses/by/4.0/>.

## REFERENCES

1. M. McLean: *Directionally Solidified Materials for High Temperature Service*, TMS, Warrendale, 1983.
2. F. Versnyder and M. Shank: *Mater. Sci. Eng.*, 1970, vol. 6, pp. 213–47.
3. J. Strickland, B. Nenchev, K. Tassenberg, S. Perry, G. Sheppard, H.B. Dong, R. Zhang, G. Burca, and N. D'Souza: *Acta Mater.*, 2021, vol. 217, 117180.
4. J. Strickland, B. Nenchev, S. Perry, K. Tassenberg, S. Gill, C. Panwisawas, H. Dong, N. D'Souza, and S. Irwin: *Acta Mater.*, 2020, vol. 200, pp. 417–31.
5. N. Siredy, M. Boufoussi, S. Denis, and J. Lacaze: *J. Cryst. Growth.*, 1993, vol. 130, pp. 132–46.
6. U. Bruckner, A. Epishin, and T. Link: *Acta Mater.*, 1997, vol. 45, pp. 5223–31.
7. W. Bogdanowicz, R. Albrecht, J. Sieniawski, and K. Kubiak: *J. Cryst. Growth.*, 2014, vol. 401, pp. 418–22.
8. J. He, F. Scholz, O. Horst, P. Thome, J. Frenzel, G. Eggler, and B. Gault: *Scr. Mater.*, 2020, vol. 185, pp. 88–93.
9. A. de Bussac and C.A. Gandin: *Mater. Sci. Eng. A*, 1997, vol. 237, pp. 35–42.
10. U. Paul, P.R. Sahm, and D. Goldschmidt: *Mater. Sci. Eng. A*, 1993, vol. 173, pp. 49–54.
11. A. Hellawell, J. Sarazin, and R.S. Steube: *Philos. Trans. R. Soc. Lond. A*, 1993, vol. 345, pp. 507–44.
12. T. Pollock and W. Murphy: *Metall. Mater. Trans. A*, 1996, vol. 27A, pp. 1081–94.
13. J. Ramirez and C. Beckermann: *Metall. Mater. Trans. A*, 2003, vol. 34A, pp. 1525–36.
14. S. Tin, T. Pollock, and W. Murphy: *Metall. Mater. Trans. A*, 2001, vol. 32A, pp. 1743–53.
15. S. Tin and T. Pollock: *Metall. Mater. Trans. A*, 2003, vol. 34A, pp. 1953–67.
16. N. Ren, C. Panwisawas, J. Li, M. Xia, H. Dong, and J. Lin: *Acta Mater.*, 2021, vol. 215, 117043.
17. N. Ren, C. Panwisawas, J. Li, M. Xia, H. Dong, and J. Lin: *J. Manuf. Proc.*, 2022, vol. 77, pp. 219–28.
18. M. Newell, K. Devendra, P. Jennings, and N. D'Souza: *Mater. Sci. Eng. A*, 2005, vol. 412, pp. 307–15.
19. N. D'Souza, M. Newell, K. Devendra, P. Jennings, M. Ardakani, and B. Shollock: *Mater. Sci. Eng. A*, 2005, vol. 413–414, pp. 567–70.
20. M. Newell, N. D'Souza, and N. Green: *Int. J. Cast Met. Res.*, 2009, vol. 22, pp. 66–69.
21. R. Napolitano and R. Schaefer: *J. Mater. Sci.*, 2000, vol. 35, pp. 1641–59.
22. T. Takaki and H. Kashima: *J. Cryst. Growth.*, 2011, vol. 337, pp. 97–101.
23. P. Soar, A. Kao, N. Shevchenko, S. Eckert, G. Djambazov, and K. Pericleous: *Phil. Trans. R. Soc. A*, 2021, vol. 380, p. 20210149.
24. B. Billia, N. Bergeon, H.N. Thi, H. Jamgotchian, J. Gastaldi, and G. Grange: *Phys. Rev. Lett.*, 2004, vol. 93, 126105.
25. P. Soar, A. Kao, G. Djambazov, and K. Pericleous: *JOM*, 2022, vol. 74, pp. 2461–69.
26. W. Xu, F. Wang, D. Ma, X. Zhu, D. Li, and A. Bührig-Polaczek: *Mater. Des.*, 2020, vol. 196, p. 109138.
27. Y. Huang, J. Shen, D. Wang, G. Xie, Y. Lu, L. Lou, and J. Zhang: *Metall. Mater. Trans. A*, 2020, vol. 51A, pp. 6364–72.
28. S. Hu, L. Liu, W. Yang, D. Sun, M. Huo, T. Huang, J. Zhang, H. Su, and H. Fu: *Metall. Mater. Trans. A*, 2019, vol. 50A, pp. 1607–610.
29. A. Rashid and J. Campbell: *Metall. Mater. Trans. A*, 2004, vol. 35A, pp. 2063–71.
30. C. Carney and J. Beech, in *Proceedings of 4th Decennial Conference on Solidification Processing*, eds. J. Beech and H. Jones, Department of Engineering Materials, University of Sheffield, 1997, pp. 33–36.
31. J. Aveson, P. Tennant, B. Foss, B. Shollock, H. Stone, and N. D'Souza: *Acta Mater.*, 2013, vol. 61, pp. 5162–71.
32. J.W. Aveson, G. Reinhart, C. Goddard, H. Nguyen-Thi, N. Manelinck-Noel, A. Tandjaoui, J.R. Davenport, N. Warnken, F. di Gioacchino, T. Lafford, N. D'Souza, B. Billia, and H.J. Stone: *Metall. Mater. Trans. A*, 2019, vol. 50A, pp. 5234–41.
33. G. Reinhart, D. Grange, L. Abou-Khalil, N. Mangelinck-Noel, N. Niane, V. Maguin, G. Guillemot, C.A. Gandin, and H. Nguyen-Thi: *Acta Mater.*, 2020, vol. 194, pp. 68–79.
34. R. Armstrong, W. Boettinger, and M. Kuriyama: *J. Appl. Crystallogr.*, 1980, vol. 13, pp. 417–24.
35. M. Rappaz and E. Blank: *J. Mater. Sci.*, 1987, vol. 22, pp. 896–906.
36. V. Randle: *Microtexture Determination and its Applications*, 2nd ed. Maney for the Institute of Materials Minerals and Mining, London, 2003.
37. L. McCartney, K. Clay, National Physical Laboratory (NPL) Report MAT 30, Rigorous Analysis for Estimating the Orientation of Cubic Crystals (2009).
38. N. D'Souza and H.B. Dong: *Scr. Mater.*, 2007, vol. 56, pp. 41–44.
39. X. Yang, D. Ness, P. Lee, and N. D'Souza: *Mater. Sci. Eng. A*, 2005, vol. 413–414, pp. 571–77.
40. X. Yang: Simulation of Stray Grain Formation in Single Crystal Ni-Based Superalloy Turbine Blades, PhD Thesis, University of London, 2005.
41. J.K. Mackenzie: *Biometrik A*, 1958, vol. 45, pp. 229–40.
42. M. Ardakani, N. D'Souza, B. Shollock, and M. McLean: *Metall. Mater. Trans. A*, 2000, vol. 31A, pp. 2887–93.
43. J. Pilling and A. Hellawell: *Metall. Mater. Trans. A*, 1996, vol. 27A, pp. 229–32.
44. R. Doherty: *Scr. Mater.*, 2003, vol. 49, pp. 1219–22.
45. N. D'Souza, B. Roebuck, D. Collins, G. West, and C. Panwisawas: *Mater. Sci. Eng. A*, 2020, vol. 773, 138862.
46. Y. Tang, N. D'Souza, B. Roebuck, P. Karamched, C. Panwisawas, and D. Collins: *Acta Mater.*, 2021, vol. 203, 116468.
47. S. Timoshenko and D.H. Young: *Elements of Strength of Materials*, 4th ed. Van Nostrand, New Jersey, 1962.
48. N. D'Souza, P. Jennings, H. Dong, X. Yang, P. Lee, and M. McLean: *Metall. Mater. Trans. B*, 2005, vol. 36B, pp. 657–66.
49. J.M. Drezet, B. Mireux, Z. Szaraz, and T. Pirling: *JOM*, 2014, vol. 66, pp. 1425–30.
50. M.B. Djurdjevic and G. Huber: *J. Alloys Compd.*, 2014, vol. 590, pp. 500–06.
51. H. Freye, M. Yasrebi, and D. Sturguis: in *Proc. 24th Annual Santa Fe Symposium*, Albuquerque, NM, 2000, pp. 1–17.
52. S.C. Huang, A.J. Elliot, M. Gigliotti, R.J. Peterson, and S.F. Rutkowski: US Patent Publication No. US 2010/0170654 A1 (2010).
53. B. Bewlay, L. Creteigny, M. Gigliotti, R.J. Peterson, A.M. Ritter, and S. Rutkowski, US Patent Publication No US 7296616 B2 (2007).
54. X. Yang, P. Lee, and N. D'Souza: *JOM*, 2005, vol. 57, pp. 40–44.
55. N. Stanford, A. Djakovic, B. Shollock, M. McLean, N. D'Souza, and P. Jennings: *Scr. Mater.*, 2004, vol. 50, pp. 159–63.

**Publisher's Note** Springer Nature remains neutral with regard to jurisdictional claims in published maps and institutional affiliations.